

PHARMACOLOGY

A unique type of GSK-3 inhibitor brings new opportunities to the clinic

Avital Licht-Murava,^{1*} Rom Paz,^{1*} Lilach Vaks,¹ Limor Avrahami,¹ Batya Plotkin,¹ Miriam Eisenstein,² Hagit Eldar-Finkelman^{1†}

2016 © The Authors, some rights reserved; exclusive licensee American Association for the Advancement of Science.

Development of protein kinase inhibitors is a focus of many drug discovery programs. A major problem, however, is the limited specificity of the commonly used adenosine triphosphate-competitive inhibitors and the weak inhibition of the more selective substrate-competitive inhibitors. Glycogen synthase kinase-3 (GSK-3) is a promising drug target for treating neurodegenerative disorders, including Alzheimer's disease (AD), but most GSK-3 inhibitors have not reached the clinic. We describe a new type of GSK-3 inhibitor, L807mts, that acts through a substrate-to-inhibitor conversion mechanism that occurs within the catalytic site of the enzyme. We determined that L807mts was a potent and highly selective GSK-3 inhibitor with reasonable pharmacological and safety properties when tested in rodents. Treatment with L807mts enhanced the clearance of β amyloid loads, reduced inflammation, enhanced autophagic flux, and improved cognitive and social skills in the 5XFAD AD mouse model. This new modality of GSK-3 inhibition may be therapeutic in patients with AD or other central nervous system disorders associated with dysregulated GSK-3.

INTRODUCTION

Protein kinases are important regulators of many biological processes, and their abnormal activity causes many human diseases (1). Development and design of specific inhibitors of protein kinases are the focus of many drug discovery programs. So far, most protein kinase inhibitors are small molecules that compete with adenosine triphosphate (ATP) for its binding site on the kinase. This type of inhibitor, although powerful, often has limited specificity (2, 3), because the ATP binding site is highly conserved among protein kinases (4, 5). This lack of specificity can be beneficial in some instances or may result in serious side effects. Another category of inhibitors are substrate-competitive inhibitors that mimic the unique interactions that occur in the less conserved substrate binding cavity of the kinase and are therefore expected to be highly selective (4, 5). Most substrate-competitive inhibitors exhibit relatively weak inhibition capacity [median inhibitory concentration (IC₅₀) values in the millimolar range] because of their weak binding to the kinase (6–9). Suicide substrate inhibitors, which bind covalently to an enzyme and irreversibly inhibit it, were described (10) but have not been reported for kinases. A substantial improvement in the binding affinity of substrate-competitive inhibitors to the kinase would result in “ideal” inhibitors that are both selective and effective.

The serine-threonine kinase glycogen synthase kinase-3 (GSK-3) is recognized as an important drug discovery target in neurodegenerative disorders, such as Alzheimer's disease (AD), multiple sclerosis, fragile X, amyotrophic lateral sclerosis, and depressive behavior (11–15). In humans, GSK-3 exists as two isozymes, GSK-3 α and GSK-3 β , which are encoded by two genes and share 97% homology in the catalytic domain (16). The mechanisms by which GSK-3 contributes to neurological disorders are under investigation. For example, GSK-3 phosphorylates the microtubule-associated protein tau (17, 18), and phosphorylated tau causes neurofibrillary tangle formation in AD (19, 20). GSK-3 also destabilizes the Wnt signaling component β -catenin (21, 22), regulates

transcription factors such as nuclear factor κ B (23, 24), activates proinflammatory factors (25, 26), and impairs autophagic and lysosomal activity (27, 28), the last of which results in the accumulation of neurotoxic or damaged proteins. Studies in animal models provide evidence of the therapeutic benefits of inhibition of GSK-3 in limiting the progression of neurodegenerative diseases and cognitive impairment (28–37). However, most GSK-3 inhibitors have not reached the clinic mainly because of limited specificity and toxic effects (11).

Previously, we described substrate-competitive GSK-3 inhibitors that inhibit both GSK-3 isozymes. These inhibitors are short phosphorylated peptides (38) that exploit the unique substrate-recognition motif of GSK-3, S¹XXXS²(p) (where S¹ is the site phosphorylated by GSK-3, and S² is the priming site phosphorylated by other kinases) (39, 40). Our previous work resulted in a leading inhibitor, L803mts, which is derived from the GSK-3 substrate heat shock factor-1 (HSF-1) (41) and has a myristic acid attached to the N-terminal end that enables cell permeability (38). In vitro and in vivo studies with L803mts showed that this compound produced therapeutic benefits in diverse disease models, including diabetes (38, 42, 43), depressive behavior (44), cancer (45), Parkinson's disease (46), AD (28), and multiple sclerosis (30). Combined mutagenesis and computational docking further revealed that the recognition of substrate combines the promiscuity of the binding loop composed of GSK-3 β residues 89 to 95 and the requirement for primed phosphorylation to enable the interaction with the phosphate-binding pocket of GSK-3 (47, 48).

During the process of improving the inhibitor L803mts, we discovered a peptide derivative, L807, that acts both as a substrate and as an inhibitor. Here, we explored the mechanism of L807 action and the activity of its myristylated version, L807mts, in a mouse model of AD. We found that L807 acts through an in situ substrate-inhibitor conversion mechanism, meaning that the peptide binds GSK-3 (α or β) and becomes phosphorylated, which converts the compound into an inhibitor. Compared with L803mts, L807mts is a more potent GSK-3 inhibitor. L807mts is also highly selective for GSK-3 in vitro, and in mice it exhibits suitable pharmacological properties, including stability, delivery to the brain, pharmacokinetics, and safety. Finally, L807mts improves neuropathological symptoms and cognitive behavior in an AD mouse model.

¹Department of Human Molecular Genetics and Biochemistry, Sackler School of Medicine, Tel Aviv University, Tel Aviv 69978, Israel. ²Department of Chemical Research Support, Weizmann Institute of Science, Rehovot 76100, Israel.

*These authors contributed equally to this work.

†Corresponding author. Email: heldar@post.tau.ac.il

RESULTS

A substrate is also a potent inhibitor

We used peptide substrates and inhibitors derived from HSF-1 (Fig. 1A). In these peptides, the priming site is Ser¹⁰ and the GSK-3 phosphorylation site is Ser⁶. Replacement of Ser⁶ with alanine produced a weak inhibition, whereas replacement of both Ser⁶ and Glu³ with alanine generated the previously described inhibitor L803 (Fig. 1A) (38). In the peptide termed L807, Glu³ is replaced with alanine, but Ser⁶ is not (Fig. 1A). We assumed that L807 would act either as a substrate or as an inhibitor, but, surprisingly, L807 has both properties. In vitro kinase assays showed that L807 is readily phosphorylated by GSK-3 β as were other GSK-3 substrates, such as the primed peptides derived from insulin receptor substrate-1 (49) or HSF-1, termed here pIRS-1 and pHSF-1 (Fig. 1B). In vitro kinase assays with pIRS-1 as the substrate for GSK-3 β in the pres-

ence or absence of L807 showed that L807 reduced GSK-3 β phosphorylation of pIRS-1 by more than 80% (Fig. 1C, left panel). The presence of pHSF-1 at a similar concentration did not inhibit pIRS-1 phosphorylation (Fig. 1C, left panel). This indicated that L807 does not inhibit GSK-3 β through substrate competition. Furthermore, comparison of GSK-3 β inhibition by L807 or L803 or their myristoylated forms, L807mts and L803mts, showed that L807 and L807mts are more potent and efficacious GSK-3 β inhibitors (Fig. 1C, middle panel). The activity assays suggested that during the process of GSK-3-mediated phosphorylation of L807, the double-phosphorylated product DpL807 (Fig. 1A) is converted into an inhibitor. Yet, externally synthesized DpL807 only slightly reduced GSK-3 β activity, and as compared to L807, its ability to inhibit GSK-3 β was negligible (Fig. 1C, right panel), indicating that DpL807 does not inhibit GSK-3 β as a “free” peptide.

Thus, we propose that the GSK-3 β /L807 complex undergoes kinase activity-dependent conformational changes that tighten the interaction of the product DpL807 with the kinase. As expected because the two isozymes share identical substrate binding site, L807mts inhibited both isozymes of GSK-3, GSK-3 β and GSK-3 α (Fig. 1D and table S1).

The substrate-inhibitor conversion mechanism of action would be predicted to result in a highly specific inhibitor. Analysis of the selectivity of L807mts for GSK-3 α or GSK-3 β using in vitro kinase assays with 139 protein kinases (Fig. 1D and table S1) demonstrated that L807mts had remarkable specificity toward both GSK-3 isozymes. Together, we have generated a new type of kinase inhibitor. The inhibitor is a substrate that is converted in situ into a potent inhibitor upon phosphorylation by the kinase.

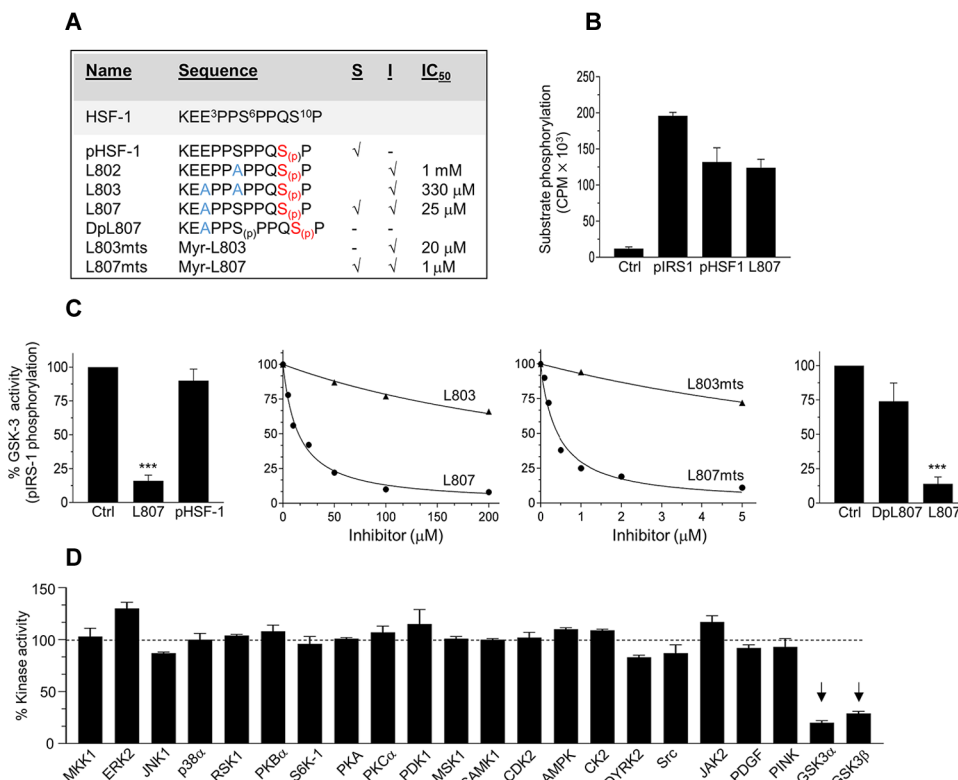


Fig. 1. L807 and L807mts function as potent GSK-3 inhibitors that act as both substrates and inhibitors. (A) List of sequences derived from the HSF-1 substrate. Positions of priming site Ser¹⁰, phosphorylation site Ser⁶, and residue Glu³ are indicated. In other sequences, S(p) indicates phosphorylated serine, and Dp indicates double phosphorylation at the priming and the GSK-3 phosphorylation sites (S⁶ and S¹⁰). The priming site is marked red, and sites mutated to alanine are marked blue. Whether the peptide functions as a substrate (S) or as an inhibitor (I) is indicated as is the IC₅₀ if relevant. L803mts and L807mts are the myristoylated forms of L803 and L807. (B) L807 is a GSK-3 substrate. GSK-3 kinase assays were performed with pIRS-1, pHSF-1, or L807 (100 μ M each). ³²P incorporation into the substrates was monitored and is presented as counts per minute (CPMs). Results are means \pm SEM of three independent experiments. Control reaction (Ctrl) does not contain substrate. (C) GSK-3 kinase assays were performed with pIRS-1 (50 μ M) as the substrate in the presence or absence of the indicated peptides (50 μ M). ³²P incorporation into pIRS-1 was monitored. Data are normalized to GSK-3 activity measured in the control reaction containing only pIRS-1. Left: The GSK-3 kinase assays were performed in the presence of L807 or pHSF-1. Middle: Dose-response curves of the inhibition of GSK-3 by a range of concentrations of L807 and L803 or L807mts and L803mts. Right: The GSK-3 kinase assays were performed in the presence of DpL807 or L807. Results are means \pm SEM of three independent experiments except the middle panels that show representative curves of three independent experiments. ****P* < 0.001 compared to Ctrl by one-way analysis of variance (ANOVA) followed by Dunnett's test. (D) Kinase assays were performed in the presence of L807mts (1 μ M). Inhibition by L807mts is presented as a percentage of each kinase activity in a control assay without L807. Results of a representative panel of protein kinases tested \pm SEM are shown. Inhibition of GSK-3 α or GSK-3 β is marked by arrows. See table S1 for complete results.

Molecular dynamics simulations of the GSK-3 β peptide complexes support an in situ substrate-inhibitor conversion

Molecular dynamics (MD) simulations were used to predict the binding modes of L807, DpL807, and DpHSF-1 (double-phosphorylated HSF-1) to GSK-3 β and to examine the possibility of in situ inhibition. We first explored the binding of L807 to GSK-3 β and then the changes that occurred upon its phosphorylation. A preliminary elastic network-based normal modes analysis of free GSK-3 β indicated that two loops showed extensive mobility: loop 63 to 69, which binds the ATP, and loop 89 to 95, which together with loop 63 to 69 delimits the promiscuous substrate binding cavity. Therefore, these loops were allowed free movement in the MD simulations together with all the side chains of GSK-3 β , the ligands [ATP or ADP

(adenosine diphosphate) and Mg^{2+}], the peptide (L807, DpL807, or DpHSF-1), and the solvent. Each MD trajectory consists of the coordinates of every atom in the system and their change over time, and the combined 100- to 150-ns trajectories provide a useful, though possibly incomplete, picture of the molecular interactions and mobility. To assess in detail the contacts in each complex, we calculated the distributions of distances between centers of mass of side chain groups of atoms (Table 1).

The time-dependent displacements of the loops and the peptide in the last 50 ns of each trajectory showed that the root mean square deviations (RMSDs) for peptides L807 and DpHSF-1 are small, and they stabilized to the same range of values in the two independent trajectories (fig. S1). However, L807 remained bound in the active site of GSK-3 β , whereas DpHSF-1 moved partially out of the active site (Fig. 2).

Snapshots from the trajectories for the three complexes, GSK-3 β /ATP/2Mg $^{2+}$ /L807, GSK-3 β /ADP/2Mg $^{2+}$ /DpL807, and GSK-3 β /ADP/

2Mg $^{2+}$ /DpHSF-1 (Fig. 2) showed that the mobility of loops 63 to 69 and 89 to 95 resembles the motion predicted independently by elastic network normal modes analysis, as well as the conformation differences observed in experimental structures of GSK-3 β [Protein Data Bank (PDB) IDs: 1H8F, 1PYX, 1O9U, 4NM3], suggesting that the MD simulations span the full range of loop motions. In at least one MD trajectory for each GSK-3 β -peptide complex (fig. S1), loop 89 to 95 is predicted to be very mobile with RMSD up to 9 to 10 Å from the equilibration position (Fig. 2B). Loop 63 to 69 is more mobile in the DpL807 complex, and to some extent also in the DpHSF-1 complex, than in the L807 complex, which may relate to predicted changes in ADP conformation and position; ADP rotates and shifts partially out of the ATP binding cavity in the DpL807 complex simulations.

The MD simulations predicted that L807 maintains a stable conformation and position within the GSK-3 β active site, in particular the extended C-terminal segment Ser 6 -Ser 10 (p) of the peptide (Fig. 2B).

Table 1. GSK-3 β /peptide and intrapeptide contacts along the MD trajectories. The numbers in parentheses indicate the percentage of time that the contact is maintained along the trajectory. Only contacts exceeding 10% of the trajectory are listed. Contacts to Lys and Arg are to their positively charged groups except when Lys_{hydr} and Arg_{hydr} are listed, which detail contacts to the hydrophobic part of these side chains. Intra-peptide contacts are listed in italics.

Residue in peptide	Contacts in trajectory 1: L807	Contacts in trajectory 2: L807	Contacts in trajectory 1: DpL807	Contacts in trajectory 2: DpL807	Contacts in trajectory 3: DpL807	Contacts in trajectory 1: DpHSF-1	Contacts in trajectory 2: DpHSF-1
Lys 1	Tyr 216 -PO $_3$ (95) S 256 (11)	Tyr 216 -PO $_3$ (100)	Tyr 216 -PO $_3$ (98)	Glu 211 (77) Ser 10 (p) (100)	Ser 6 (p) (91) Ser 10 (p) (100)	Tyr 216 -PO $_3$ (99)	—
Lys 1 _{hydr}	—	—	—	—	Val 180 (24)	Pro 7 (75)	—
Glu 2	—	Tyr 221 (12)	—	Arg 92 (23)	—	—	—
Ala 3 /Glu 3	Ser 66 (11) Pro 7 (15) Pro 8 (18)	Pro 5 (16)	Ile 217 (80) Pro 5 (50)	—	Ser 66 (8) Phe 67 (8)	—	—
Pro 4	—	Tyr 216 _{ring} (26)	Ile 217 (39) Ser 203 (86)	Pro 8 (52)	Phe 67 (73) Phe 93 (19) Pro 8 (29)	—	—
Pro 5	Ser 66 (10) Ser 219 (14)	Ala 3 (16)	Val 214 (22) Tyr 216 _{ring} (17) Ala 3 (50) Pro 7 (5) Pro 8 (8)	Pro 7 (10) Pro 8 (89)	Phe 67 (45) Phe 93 (57) Pro 8 (25)	—	—
Ser 6 /Ser 6 (p)	ATP P $^{\gamma}$ (72) Asp 181 $^{\gamma}$ (87) Lys 183 (77) Lys 203 (50)	ATP P $^{\gamma}$ (93) Asp 181 $^{\gamma}$ (50) Lys 183 (100) Ser 219 (98)	Lys 94 (91) Arg 96 (100) Arg 180 (100) Lys 205 (100)	Arg 96 (100) Arg 180 (100) Lys 205 (100)	Arg 96 (100) Arg 180 (86) Lys 205 (99) Lys 1 (91)	Lys 183 (98)	Lys 183 (92) Gln 185 (40) Ser 219 (27)
Pro 7	Ile 217 (64) Tyr 216 _{ring} (71) Ala 3 (15)	Ile 217 (82) Tyr 216 _{ring} (98)	Pro 5 (5) Pro 11 (92)	Phe 67 (11) Phe 93 (90) Pro 5 (10)	Arg 96 _{hydr} (44)	Tyr 216 _{ring} (98) Ile 217 _{ring} (15) Lys 1 _{hydr} (75)	Tyr 216 _{ring} (99) Ile 217 _{ring} (45)
Pro 8	Phe 67 (22) Ala 3 (18)	—	Val 214 (55) Pro 5 (8)	Arg 92 _{hydr} (54) Phe 93 (40) Pro 4 (52) Pro 5 (89)	Phe 67 (45) Val 187 (27) Phe 93 (97) Pro 4 (29) Pro 5 (25)	—	—
Gln 9	Arg 96 (99) Arg 180 (78)	Arg 96 (98) Arg 180 (56)	Pro 12 (27)	Lys 205 (89)	Arg 92 (75) Phe 93 (75)	Arg 96 (89) Arg 180 (34)	Arg 96 (74) Arg 180 (65)
Ser 10 (p)	Arg 96 (98) Arg 180 (100) Lys 205 (98)	Arg 96 (100) Arg 180 (100) Lys 205 (99)	Lys 94 (88) Lys 205 (100) Asn 213 (68)	Lys 94 (100) Lys 205 (100) Lys 1 (100)	Arg 92 (20) Arg 96 (100) Lys 205 (100) Lys 1 (100)	Arg 96 (94) Arg 180 (100) Lys 205 (100)	Arg 96 (97) Arg 180 (100) Lys 205 (99)
Pro 11	—	—	Pro 7 (92)	Arg 92 _{hydr} (11)	Lys 94 _{hydr} (32)	—	—

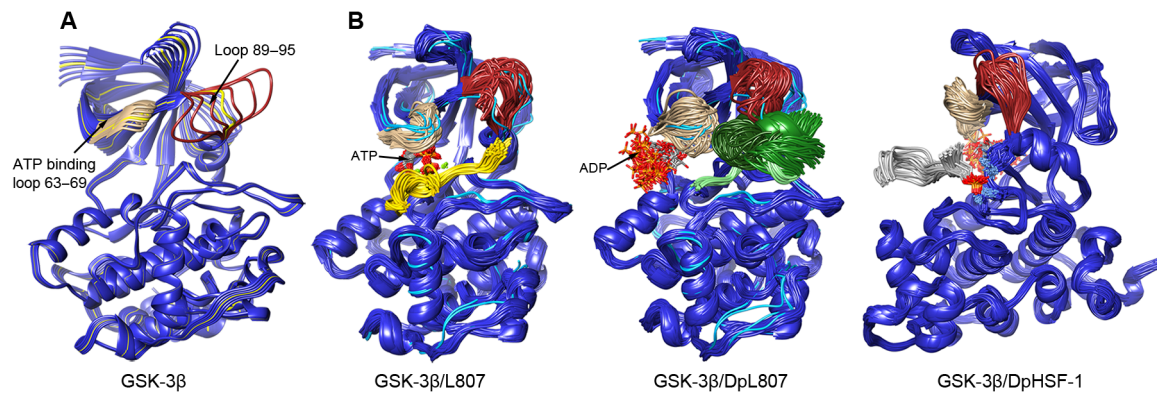


Fig. 2. Binding of L807, DpL807, or DpHSF-1 to GSK-3 β . (A) Elastic network-based normal mode 3, calculated for free GSK-3 β . The mobile loops 63 to 69 and 89 to 95 are shown in beige and reddish brown, respectively. The yellow ribbon depicts the crystallographic structure (PDB ID: 1H8F). (B) Clusters of MD snapshots taken every 2 ns from the production trajectories of the L807 complex, DpL807 complex, and DpHSF-1 complex. Loops 63 to 69 and 89 to 95 are colored as in (A). The light blue ribbons are superposed experimental structures of GSK-3 β in complex with Hepes (PDB ID: 1H8F), an ATP analog (PDB ID: 1PYX), or ADP and an inhibitory peptide (PDB ID: 4NM3), and GSK-3 β phosphorylated on Tyr²¹⁶ in complex with an ATP analog (PDB ID: 1O9U). L807 is shown in yellow. DpL807 from the three trajectories is shown in three shades of green to emphasize the conformation change and shift within the substrate binding trough. DpHSF-1 is in gray. The view of the DpHSF-1 complex was rotated about the vertical axis by $\sim 90^\circ$ relative to the other structures to show the dissociation of the N-terminal part of the peptide.

The binding is dominated by the electrostatic interaction between L807/Ser¹⁰(p) and GSK-3 β residues Arg⁹⁶, Arg¹⁸⁰, and Lys²⁰⁵, which form the positively charged binding pocket for the phosphorylated priming site (Table 1, Fig. 3A, and fig. S2A) (50, 51). Additional stable interactions include contacts with the hydrophobic patch of GSK-3 β (fig. S2B), which we previously identified as an inhibitor binding site (47, 48). The distance between atoms L807/Ser⁶ O γ and ATP P γ is 5 Å or less for 82% of the time (Table 1 and fig. S2C), adequate for phosphorylation, consistent with L807 binding to GSK-3 β as a substrate. Hence, the MD simulation results predicted that L807 binds predominantly to the C-terminal lobe of the kinase with residue Ser⁶ positioned for phosphorylation, making only few contacts with loop 63 to 69 and no contacts with loop 89 to 95.

The three MD trajectories for the complex GSK-3 β /ADP/2Mg²⁺/DpL807 show that DpL807 changes conformation and shifts within the substrate binding trough of GSK-3 β (Fig. 2B). A prevalent occurrence in all three trajectories is the formation of a helical turn by DpL807 residues Ser⁶-Gln⁹ (Fig. 3B), which is stabilized by interactions of both Ser⁶(p) and Ser¹⁰(p) with the GSK-3 β positively charged cavity and with positively charged residues in loop 89 to 95 (Table 1 and fig. S3, A and B). Thus, Ser⁶(p) inserts into the positive cavity, whereas Ser¹⁰(p) shifts to the edge of the cavity. Analysis of the time dependence of the distance between Phe⁶⁷ in one loop and Phe⁹³ in the other mobile loop of GSK-3 β indicated that these two loops approach one another in the DpL807 complex (fig. S3C) but not in the L807 complex (fig. S2D). Phe⁹³ also contacts DpL807 residues Pro⁷ and Pro⁸ (fig. S3D). In two trajectories, the N-terminal segment of DpL807 forms a hairpin turn (Fig. 3B, middle and bottom panels), creating a hydrophobic center stabilized by intrapeptide interactions between Pro⁴, Pro⁵, Pro⁷, and Pro⁸ (fig. S3E). The third trajectory predicts that a second helical turn is formed; DpL807 also shifts into the “promiscuous” substrate binding pocket that we described previously (47, 48) and is located between loops 63 to 69 and 89 to 95 (Fig. 3B, bottom panel), contacting GSK-3 β residues Phe⁶⁷, Val⁸⁷, and Phe⁹³ (fig. S3D). The hydrophobic center of DpL807 is maintained all along this trajectory.

In summary, the trajectories for the GSK-3 β /ADP/2Mg²⁺/DpL807 complex provide snapshots that predict an in situ transformation of DpL807. The transformation starts with the formation of the Ser⁶(p)-

Gln⁹ helical turn and the shift of Ser⁶(p) into the positively charged cavity of GSK-3 β and is followed with the formation of the Glu²-Pro⁵ hairpin and the creation of a hydrophobic center. Finally, a second helical turn is formed. During these changes, the peptide gradually shifts within the active site, away from the hydrophobic patch and into the substrate binding pocket delimited by GSK-3 β loops 63 to 69 and 89 to 95. This predicted transformation indicated that the inhibitory effect of DpL807 appears to arise from the formation of a stable hydrophobic center in the peptide, binding of the two phosphorylated serine residues in and near the positively charged cavity, and the formation of hydrophobic contacts with the substrate binding pocket, particularly with GSK-3 β residue Phe⁹³.

From the in situ inhibition model of DpL807, we can begin to address the question: Why does phosphorylation of the peptide DpHSF-1, which differs from DpL807 only in position 3, Glu³ instead of Ala³, not produce a similar inhibitory effect? The MD simulations predicted that, unlike DpL807, DpHSF-1 does not form a helical turn and its N-terminal part shifts out of the kinase binding trough (Fig. 2B and Table 1). Furthermore, the DpHSF-1 residue Ser⁶(p) does not approach the positively charged cavity where Ser¹⁰(p) is positioned. Thus, the simulations predicted that DpHSF-1 does not undergo the conformation change seen for DpL807, because the negative Glu³ is repelled from Ser⁶(p) and Ser¹⁰(p). Instead, Ser⁶(p) moves away from GSK-3 β residues Asp²⁰⁰ and Asp¹⁸¹, resulting in partial dissociation. The final dissociation step, which requires breaking the interaction with the positively charged cavity of GSK-3 β , is probably a much slower process and is not seen in any of our simulations.

According to the predicted L807 binding and inhibition model, we expected that the binding and phosphorylation of L807 will not involve interactions with GSK-3 β Phe⁹³, whereas inhibition by L807 will require these interactions. We thus tested these predictions using the GSK-3 β mutant F93A in which Phe⁹³ was mutated to alanine (47) for in vitro phosphorylation and inhibition assays. F93A readily phosphorylated L807 but was not inhibited by L807 (Fig. 3C). Hence, the binding and phosphorylation of L807 were not affected by the F93A mutation; however, the extensive interactions with Phe⁹³ formed after L807 phosphorylation cannot occur in the F93A mutant, resulting in destabilization of the inhibitory GSK-3/DpL807 complex.

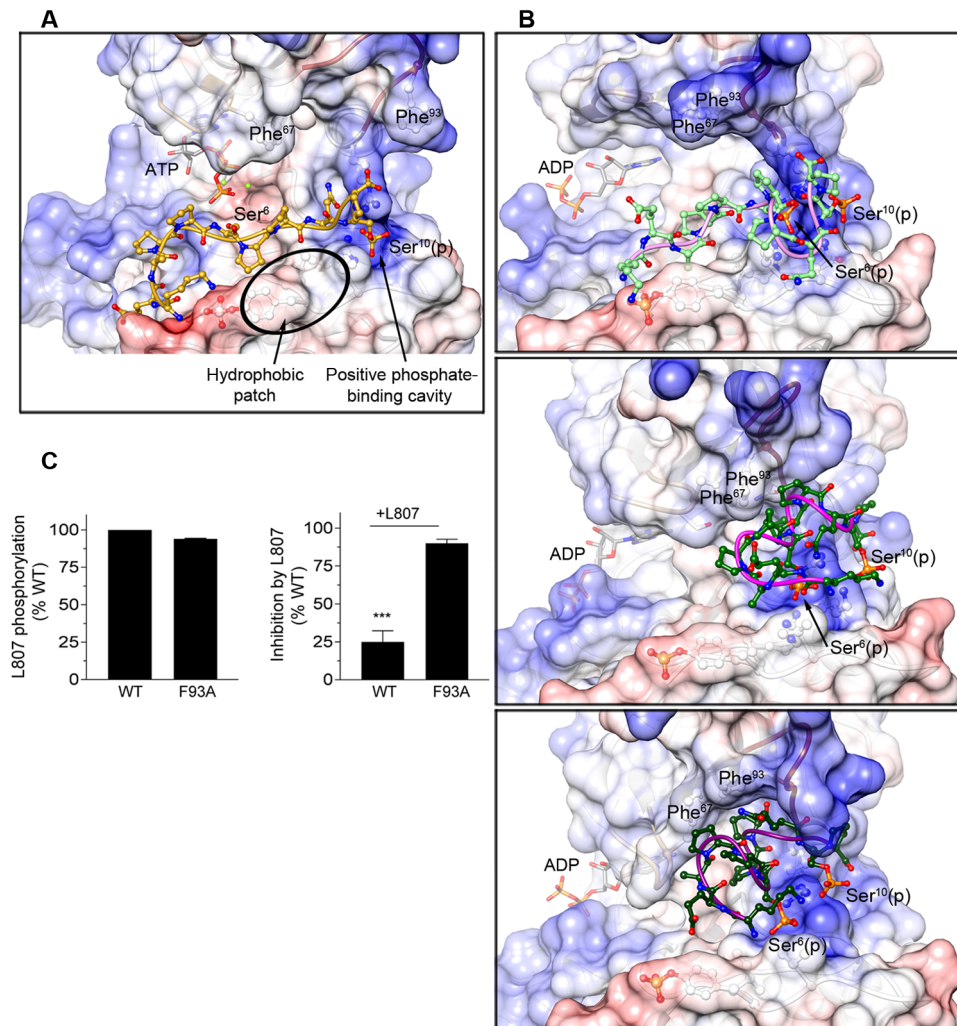


Fig. 3. L807 substrate binding, the conformational change of DpL807 that produces inhibitory binding, and the effect of mutation GSK-3 β F93A. (A) Binding mode of L807. The peptide is shown in gold with red oxygen atoms, blue nitrogen atoms, and orange phosphor atom. Ser¹⁰(p) is located in the positively charged cavity, and Ser⁶ points toward the γ -phosphate of ATP. (B) Steps in the structural change in DpL807 that support the proposed in situ inhibition. The top panel shows the formation of a helical turn in the C-terminal part and the binding of Ser⁶(p) in the positive cavity and of Ser¹⁰(p) near this cavity. The middle panel presents the bending of the N-terminal part, the detachment from Tyr²¹⁶(p), and the formation of a hydrophobic center. The bottom panel presents the formation of a second helical turn and the shift into the cavity delimited by loops 63 to 69 and 89 to 95. In (A) and (B), the surface of GSK-3 β is colored by the electrostatic potential: blue for positive, red for negative, and white for neutral. The surface is transparent to show the residues that interact with the peptide. (C) Phe⁹³ is required for inhibition. Left: GSK-3 β kinase assays were performed with WT GSK-3 β or F93A mutant using L807 as a substrate. ³²P incorporation into L807 was monitored. Data are normalized to maximal activity of WT. Right: GSK-3 β kinase assays were performed with WT or F93A with L807 (50 μ M) using pIRS-1 (50 μ M) as a substrate. ³²P incorporation into pIRS-1 was monitored. Data are normalized to maximal activity of WT with no inhibitor. Results are means \pm SEM. *** P < 0.001 by Student's t test.

L807mts inhibits GSK-3 in cells and in animals

The high selectivity and potency of L807mts in the assay with purified GSK-3 prompted us to evaluate its biological properties. We exposed human neuroblastoma SH-SY5Y cells to a range of concentrations of L807mts and measured the abundance of β -catenin, which is a Wnt signaling component that is destabilized upon phosphorylation by GSK-3 (21, 52). L807mts increased β -catenin abundance in cells at a concentration as low as 5 μ M (Fig. 4A). In addition, tyrosine phosphorylation of GSK-3 α and GSK-3 β at residues Tyr²⁷⁶ and Tyr²¹⁶, respectively, was significantly reduced by exposing the cells to L807mts (Fig. 4A). The relative weak response in GSK-3 autophosphorylation could be explained by the fact that L807mts does not block the ATP binding site and thus enables phosphate transfer to the GSK-3 tyrosine residue.

Nevertheless, L807mts binding to the catalytic cavity likely slows down the kinetics of autophosphorylation. Another marker for GSK-3 inhibition is enhanced lysosomal acidification (27, 28). Mouse embryonic fibroblast (MEF) cells that lack presenilin proteins (MEF-PS1/2^{-/-} cells) are deficient in lysosomal acidification (53, 54). Exposing MEF-PS1/2^{-/-} cells to L807mts or L803mts restored lysosomal acidification, as detected in live cells stained with LysoTracker Red, a fluorescent dye that accumulates in acidified organelles (Fig. 4B). However, L807mts was more potent (Fig. 4B). In hippocampal primary neurons, exposure to L807mts also increased lysosomal acidification (Fig. 4C).

We also conducted a series of in vivo experiments using C57BL/6J mice that were administered L807mts intranasally at doses ranging from 20 to 80 μ g per mouse. We chose the nasal route, because this

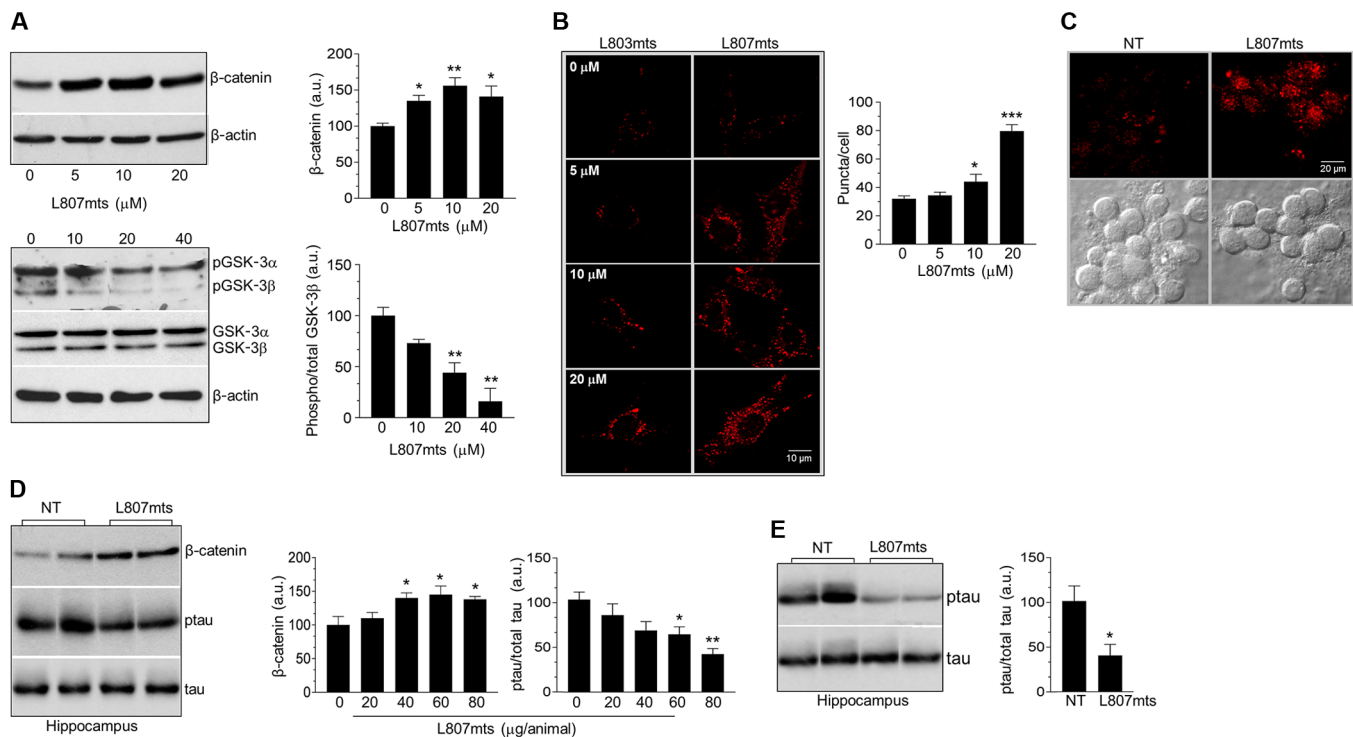


Fig. 4. L807mts is a potent GSK-3 inhibitor in cells and animals. (A) The effect of L807mts on β -catenin abundance or tyrosine phosphorylation of GSK-3 α/β . SH-SY5Y cells were treated with indicated concentrations of L807mts for 2.5 hours, and protein abundance was determined by Western blotting with antibodies recognizing the indicated proteins. The right panel shows densitometry analyses. Results are means \pm SEM of three independent experiments. * $P < 0.05$, ** $P < 0.01$ compared to control by one-way ANOVA with Dunnett's test. (B) The effect of L807mts on lysosomal pH. MEF-PS1/2^{-/-} cells were treated with indicated concentrations of L803mts or L807mts for 2.5 hours. Cells were stained with LysoTracker Red, and live cells were imaged by confocal microscopy. Red dots indicate low-pH compartments, likely representing acidic lysosomes. Graph shows quantitation of low-pH puncta in the cells. Results are means \pm SEM of dots per cell from the analysis of at least 50 cells from five fields per condition. * $P = 0.012$, *** $P = 0.001$ compared to control by one-way ANOVA with Dunnett's test. (C) Effect of L807mts on lysosomal acidification of hippocampal neurons. Hippocampal primary neurons prepared from newborn mice were exposed to 20 μ M L807mts for 2.5 hours, then stained with LysoTracker Red, and visualized by confocal microscopy. The field is mainly focused at the soma plane. Data are representative of three independent experiments. (D) The effect of L807mts on GSK-3 activity in the mouse brain. C57BL/6J mice were treated nasally with L807mts at indicated doses for two successive days. Hippocampal tissue extracts were immunoblotted for the amount of β -catenin and tau phosphorylation at Ser³⁹⁶. The left panel shows a representative gel obtained from each of two animals treated with 60 μ g of L807mts or nontreated (NT). The right panel shows densitometry analyses. Results are means \pm SEM obtained from four animals. For β -catenin: * $P = 0.03$ for 40 μ g, * $P = 0.016$ for 60 μ g, * $P = 0.04$ for 80 μ g, treated versus nontreated. For tau: * $P = 0.037$ for 60 μ g, ** $P = 0.0014$ for 80 μ g, treated versus nontreated, by one-way ANOVA with Dunnett's test. (E) Transgenic mice that express human mutant tau were treated with 60 μ g of L807mts or nontreated, and tissue extracts were analyzed as described in (D). The right panel shows densitometry analyses. Results are means \pm SEM obtained from four animals. * $P = 0.01$, treated versus nontreated, by Student's *t* test. a.u., arbitrary units.

route is an effective delivery route for L803mts and other peptide-based compounds (28, 30, 55, 56). The mice were treated with two doses of L807mts in two consecutive days and were harvested 4 hours after the administration of the second dose. We then dissected hippocampal tissues and measured the abundance of β -catenin and the amount of tau phosphorylation at Ser³⁹⁶, which is a site-phosphorylated GSK-3 (17, 57, 58). Treatment of mice with L807mts increased β -catenin abundance and reduced tau phosphorylation in the hippocampus (Fig. 4D). Similarly, L807mts reduced the phosphorylation of the human mutant tau K257T/P301S (Fig. 4E) expressed in the brains of transgenic mice that exhibit phenotypes similar to frontotemporal dementia in humans (59). Collectively, these data indicated that L807mts is a potent GSK-3 inhibitor in cells and in animals.

L807mts shows acceptable pharmacological properties

The potency and selectivity of L807mts prompted us to evaluate its pharmacological properties. We generated fluorescently labeled Cy5-L807mts to enable in vivo detection. To evaluate stability, we incubated Cy5-L807mts with freshly prepared mouse serum at 37°C for times ran-

ging from 5 min to 2 days and monitored the stability of Cy5-L807mts by gel electrophoresis. No degradation was observed after 48 hours in serum (Fig. 5A). Digestion of Cy5-L807mts with trypsin or with proteinase K served as control for the detectability of cleaved Cy5-L807mts (Fig. 5A). We conducted pharmacokinetic analyses in mice injected intravenously with Cy5-L807mts. We quantified Cy5-L807mts stability in blood using fluorescence (Fig. 5B, lower panel) or qualitatively visualized Cy5-L807mts by gel electrophoresis (Fig. 5B, upper panel). Cy5-L807mts was stable in circulation for up to 12 hours after injection, and clearance from the blood stream after intravenous injection occurred with a half-life of 5 to 6 hours. We detected the cleaved products of Cy5-L807mts in urine 10 and 12 hours after injection (Fig. 5C). Because the brain is the relevant target for AD treatment, we evaluated Cy5-L807mts delivery to the brain by imaging the brains immediately after killing at times ranging from 2 to 12 hours after intravenous administration. Fluorescence signal peaked at 4 hours, and the Cy5-L807mts was cleared from the brain at 12 hours after administration (Fig. 5D).

Finally, we performed toxicological studies after intraperitoneal or intranasal administration of 600 μ g of L807mts, a dose about 10-fold

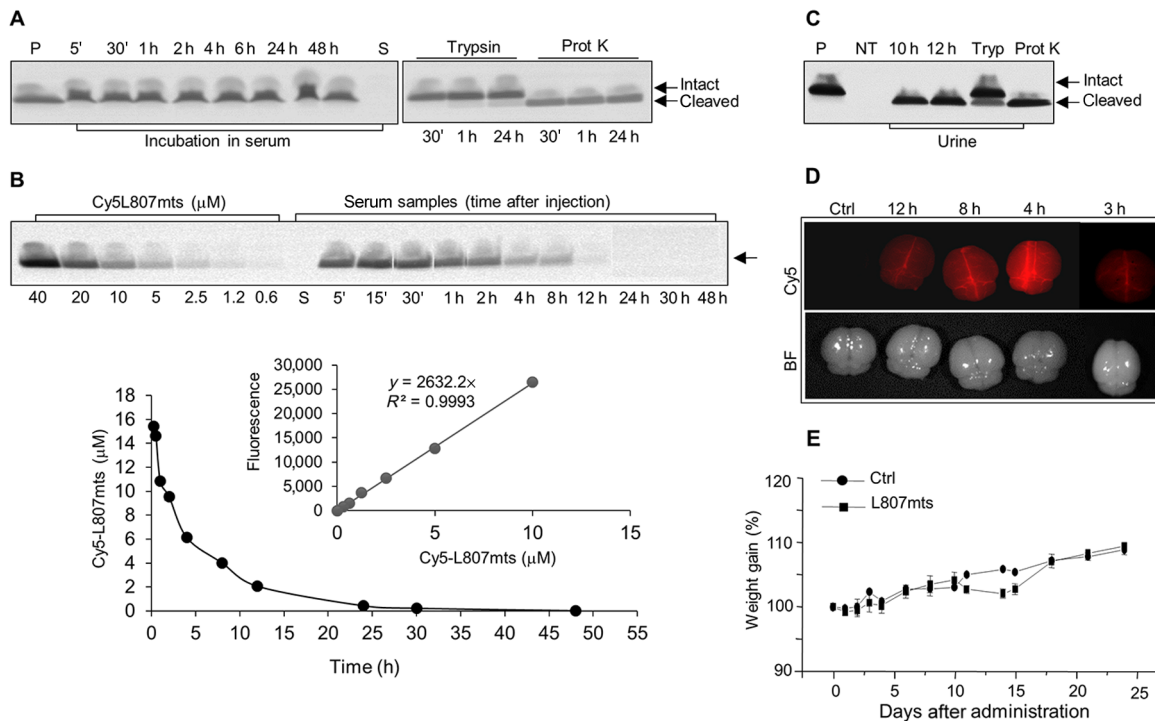


Fig. 5. Pharmacological properties of L807mts. (A) The stability of L807mts in serum. Cy5-L807mts (10 μ M) was incubated in fresh mouse serum for indicated times at 37°C. Samples were separated by gel electrophoresis and imaged using an FLA-5100 analyzer. Control peptide that was not exposed to serum is indicated by “P” and marked as “intact.” Products of trypsin or proteinase K (Prot K) digestion are indicated as “cleaved.” Serum from nontreated animals is marked as “S.” A representative gel of three independent experiments is shown. (B) The half-life of Cy5-L807mts in circulation. Four mice were given 60 μ g of Cy5-L807mts intravenously. Blood samples were collected at indicated time points. The upper panel shows samples that were separated on the same gel and imaged after gel electrophoresis. Samples were analyzed in a microplate fluorescence reader, and half-life (5 to 6 hours) was calculated on the basis of calibration curve (inset). A representative gel of three independent experiments is shown. (C) Excretion of CY5-L807mts in urine. Urine samples were collected from four mice 10 and 12 hours after intravenous administration of 60 μ g of Cy5-L807mts. Samples were analyzed by gel electrophoresis. Digestion products obtained with trypsin (Tryp) or proteinase K (Prot K), pure peptide (P), and control animal urine not receiving Cy5-L807mts (NT) are shown. (D) Penetration of Cy5-L807mts into the brain. Twelve mice were treated with 100 μ g of Cy5-L807mts intravenously. After killing at indicated times and perfusion with phosphate-buffered saline (PBS), brains were removed and immediately imaged using the CRI Maestro fluorescence imaging system. Representative bright-field (BF) and Cy5 images are shown. (E) Toxic effects of L807mts. Mice were treated or not treated with 600 μ g of L807mts per animal, a dose that is 10-fold of the optimal dose (60 μ g per animal). Body weight was monitored as indicated over 24 days. Results are means \pm SEM (n = 4 nontreated or 6 treated mice). See table S2 for additional metrics of toxicity.

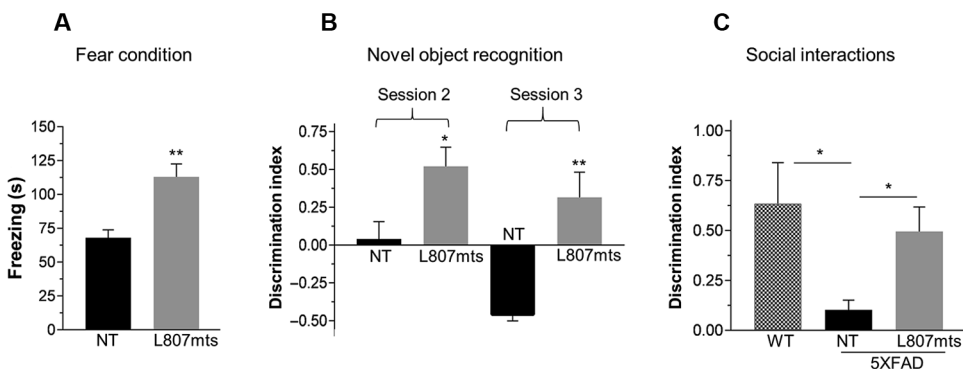


Fig. 6. L807mts reverses cognitive decline and impaired social skills in the 5XFAD AD mouse model. 5XFAD mice were treated nasally with L807mts and then subjected to behavioral tests. (A) In the fear conditioning test, freezing-time duration in mice treated with L807mts compared to nontreated mice was determined 24 hours after the electric stimulus. Results are means \pm SEM (n = 6). Means: 113 and 68.05. Medians: 115.5 and 68.92. $^{***}P$ = 0.0025, treated versus nontreated, by Student’s t test. (B) In the object recognition test, the discrimination index of nontreated or treated mice was determined in two sessions (session 2 and session 3) as described in Materials and Methods. Results are means \pm SEM (n = 5). Means: 0.52, 0.04, 0.315, and -0.448 . Medians: 0.51, -0.02 , 0.42, and -0.52 . $^{*}P$ = 0.0294, $^{***}P$ = 0.0019 for treated versus nontreated in session 2 or session 3, respectively, by Student’s t test. (C) In the sociability test, the discrimination index was determined in WT C57BL6/J mice and in the 5XFAD mice that were treated or not treated with L807mts. Results are means \pm SEM (n = 4). Means: 0.635, 0.05, and 0.495. Medians: 0.635, 0.08, and 0.475 for WT, nontreated, or treated 5XFAD mice, respectively. $^{*}P$ = 0.040, WT versus 5XFAD mice; $^{*}P$ = 0.026, 5XFAD mice treated versus nontreated, by Student’s t test.

higher than the effective concentration. Body weight, neurological symptoms, and mortality were analyzed at intervals over the 25 days after administration (table S2), and no adverse effects were observed as shown for changes in body weight (Fig. 5E). Together, these data showed that L807mts is stable, delivered to the brain, and nontoxic under conditions tested here.

L807mts reverses cognitive decline in an AD mouse model

GSK-3 drives neurodegenerative disease progression in several models, including those of AD (28–37). Furthermore, GSK-3 inhibition enhances cognitive ability in mouse models of AD (28, 29, 33, 37). We thus used the AD model of the 5XFAD mice to evaluate the therapeutic activity of L807mts on both neuropathology and cognitive functions. These mice express genes encoding amyloid precursor protein

and presenilin-1 (PS1) with mutations characteristic of familial AD and develop massive cerebral β amyloid ($A\beta$) loads and memory deficits (60). At 2 months of age, we began treating mice nasally with L807mts (60 μ g per dose), or vehicle, every other day for 120 days. At 6 months of age, we subjected the mice to cognitive and behavioral tests.

The contextual fear conditioning test evaluates associative learning and memory. As reported previously, 5XFAD mice show reduced “freezing time” duration as compared to wild-type (WT) mice (28, 60). Treatment with L807mts improved performance compared to that of nontreated mice (Fig. 6A). The novel object recognition test evaluates recognition memory. In this test, the spontaneous tendency of the mouse to explore a novel object rather than a familiar one is evaluated (61, 62). The nontreated 5XFAD mice spent about equal time at the novel and the familiar objects, whereas the L807mts-treated animals spent significantly more time near the novel object (Fig. 6B, session 2). The next test was conducted 24 hours later, and the previously used

familiar object was replaced by a new object (“session 3”). The untreated animals preferred to spend more time near the object that they had seen before, as manifested by the negative values obtained for the discrimination index (Fig. 6B, session 3). In contrast, the L807mts-treated animals spent more time near the new object (Fig. 6B, session 3). This tendency of the AD mice to spend more time with a familiar object is similar to repetitive or stereotypic behavior common in AD patients (63, 64). Thus, L807mts improved memory and reversed the repetitive or stereotypic behavior.

Excess GSK-3 activity is associated with impaired social interactions in rodents (65–67). We therefore evaluated sociability of the 5XFAD mice using the “three-apparatus” sociability test (68, 69). This test monitors how much time the subject mouse spends near a “stranger” mouse. Preference for interaction with the stranger serves as an index for sociability. The 5XFAD mice were less sociable than the WT mice (Fig. 6C). L807mts-treated mice clearly preferred to spend more time

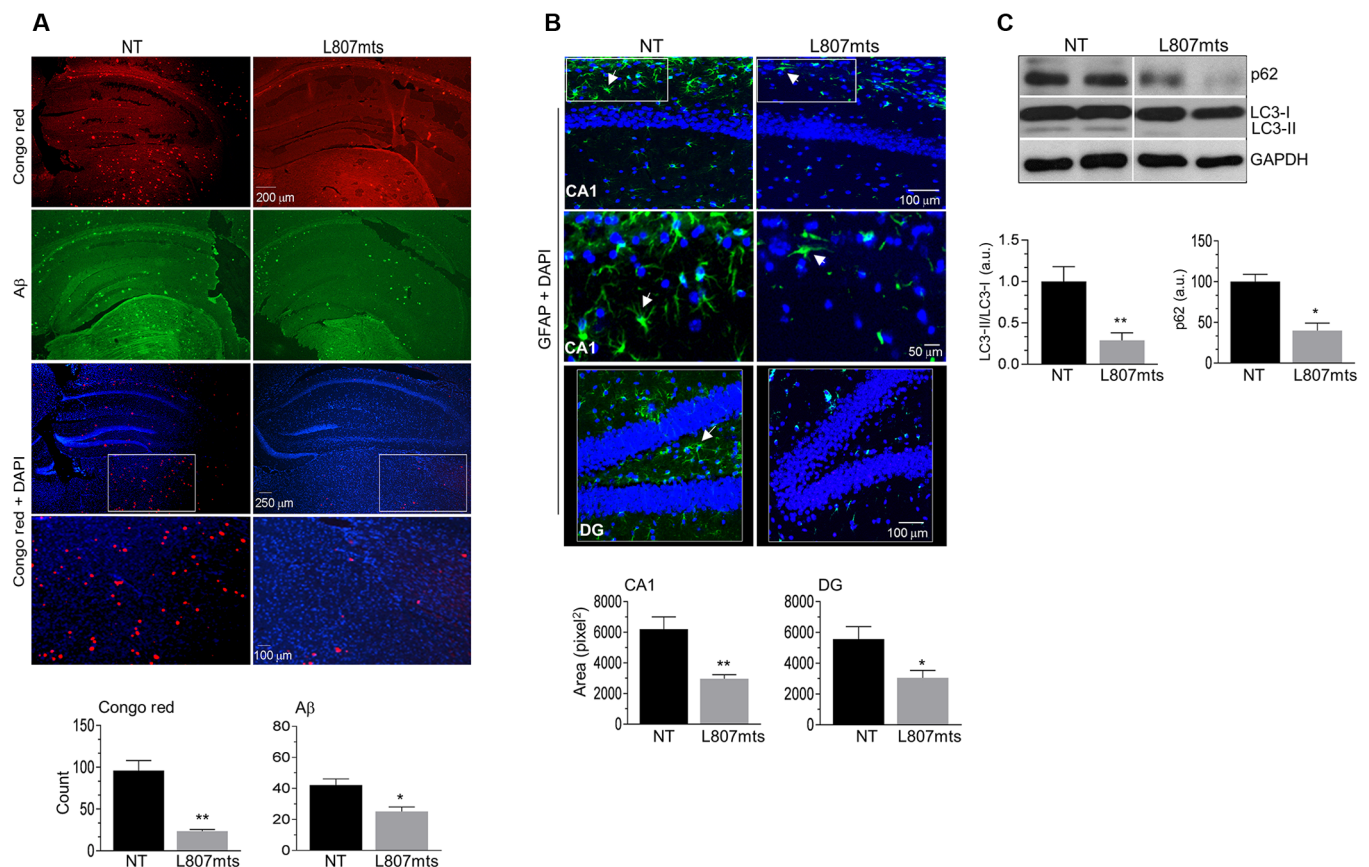


Fig. 7. L807mts treatment clears $A\beta$ deposits, reduces astrogliosis, and is associated with increased autophagic activity. (A) L807mts reduces $A\beta$ pathology. Representative histological images of paraformaldehyde-fixed hemibrain sections obtained from L807mts-treated or nontreated 5XFAD mice. Congo red staining, immunostaining with the $A\beta$ antibody (6E10), and Congo red plus 4',6-diamidino-2-phenylindole (DAPI) stains are shown. Magnified area is shown at the lower panel. Quantitation of plaques is shown at the lower panel; the means \pm SEM of three slices from each group ($n = 3$) are plotted. For Congo red, values are as follows. Means: 23.67 and 96.11. Medians: 24.5 and 88, treated versus nontreated, respectively. $**P = 0.0037$ by Student's t test. For $A\beta$, values are as follows. Means: 25.11 and 42.17. Medians: 25.33 and 39, treated versus nontreated, respectively. $*P = 0.025$ by Student's t test. (B) L807mts reduces astrogliosis. Brain tissue sections from L807mts-treated or nontreated animals were immunostained with an antibody against GFAP and DAPI dye. Images were taken for CA1 (upper two rows of images) and dentate gyrus (DG, lower row) hippocampal regions. Magnified area shows astrocytes marked with arrowheads. Quantitation of astrocytes is shown at the lower panel; results are means \pm SEM of three slices from each group ($n = 4$). For CA1, values are as follows. Means: 2967 and 6213. Medians: 2891 and 6052, treated versus nontreated, respectively. $**P = 0.0084$ by Student's t test. For dentate gyrus, values are as follows. Means: 3062 and 5565. Medians: 2689 and 5195, treated versus nontreated, respectively. $*P = 0.0365$ by Student's t test. (C) Amounts of p62 (also known as SQSTM1), LC3-I, and LC3-II were determined in hippocampal tissue extracts from L807mts-treated or nontreated animals by immunoblot analysis. Densitometry analysis is shown at the lower panel. Results plaques are means \pm SEM obtained from five brains. $*P = 0.017$, $**P = 0.0075$ for p62 or LC3I/LC3II, respectively, treated versus nontreated, by Student's t test. GAPDH, glyceraldehyde phosphate dehydrogenase.

near the stranger than in other chambers as compared to the nontreated group (Fig. 6C). Collectively, these experiments showed that treatment with L807mts improves cognitive and social behavior in the mouse model of AD.

L807mts reduces A β pathology and increases autophagic activity in AD mouse model

Increased production of peptides of A β and accumulation of A β plaques are key hallmarks of AD pathogenesis (70–72). The accumulation of A β aggregates results at least in part from impaired cellular clearance manifested by reduced autophagic and lysosomal activity (73–75). Given that GSK-3 is a key regulator of autophagy and lysosomal function (27, 28) and that L807mts enhances lysosomal acidification (Fig. 4, B and C), we evaluated A β loads in untreated and L807mts-treated 5XFAD mice. Brain tissue sections were stained with Congo red dye that stains amyloid fibrils or with a specific A β monoclonal antibody. In the brains of untreated mice, Congo red staining and A β immunostaining detected pronounced abundance of A β aggregates (Fig. 7A). In contrast, the brains from mice treated nasally with L807mts had a significant reduction in both Congo red staining and A β immune staining, indicating reduction in A β accumulation and fibril formation (Fig. 7A).

Increased A β loads activate proinflammatory responses and astroglia (76–78). To compare numbers of astrocytes in treated and untreated brains, we stained brain tissue sections for GFAP, a glial fibrillary acidic protein that is a specific marker for astrocytes. Intranasal treatment with L807mts significantly reduced the number of astrocytes in both the CA1 and dentate gyrus sections of the hippocampi (Fig. 7B).

Finally, we analyzed autophagic markers in the hippocampi of treated and untreated animals. These markers included p62 (also known as SQSTM1), which interacts with ubiquitinated proteins and is degraded upon increased autophagic flux, and the microtubule-associated protein light chain 3-II (LC3-II), a protein that is associated with autophagosome membranes, is also reduced in abundance under conditions of increased autophagic flux (73–75). The hippocampi of L807mts-treated mice had significantly less p62 and LC3-II compared to those from sham-treated 5XFAD mice (Fig. 7C). This indicated that L807mts enhanced autophagic activity as reflected by increased turnover of the autophagosomal marker LC3-II and cargo delivery protein p62. Hence, this L807mts-induced enhancement in autophagic flux may be partially responsible for the A β clearance observed in this AD model.

DISCUSSION

Many potent GSK-3 inhibitors have been reported; however, most of them did not advance to clinical trials. There could be multiple reasons for this failure. Most GSK-3 inhibitors are ATP-competitive inhibitors, which potentially could also inhibit other kinases, thus limiting their effective dosage. Moreover, some of them had only limited oral bioavailability. Substrate-competitive inhibitors for protein kinases offer promising therapeutic opportunities with improved specificity and fewer off-target side effects. However, rational design and development of substrate-competitive inhibitors are complicated, because knowledge of the recognition modes of substrates is essential but not sufficient. The substrate forms specific though weak interactions with the enzyme; thus, copying these interactions does not guarantee inhibition. Although all substrate-competitive inhibitors reported are based on the idea of “phosphorylation-invalid” substrate, namely, peptide sequences that cannot be phosphorylated, here we present a different concept of a

“dissociation-invalid” or “dissociation-resistant” substrate. Namely, the inhibitor acts as a substrate, but, in contrast to regular substrates, its phosphorylation prevents or slows down its dissociation from the kinase. This requirement for kinase activity to produce inhibition might be an advantage, because it might spare less active or inactive GSK-3 in healthy tissues.

A similar concept can be found in suicide substrates, which covalently bind to the enzyme after catalysis (10). These substrates are small molecules and inhibit the enzyme in an irreversible manner. In contrast, L807 is a peptide that undergoes phosphorylation and does not appear to become covalently attached to the kinase after catalysis.

We found that substrate-to-inhibitor conversion is facilitated by (i) the presence of an Ala at position 3 in the peptide, which impairs the dissociation of DpL807; (ii) the presence of the SXXXS(p) motif, which can undergo conformational changes that facilitate binding of two phosphate groups near the GSK-3 phosphate-binding pocket; and (iii) the presence of two sites that facilitate binding of the inhibitor. In GSK-3, the “positive” phosphate-binding pocket binds the doubly phosphorylated DpL807, and the promiscuous pocket can accommodate DpL807 and stabilize its binding through interactions with the hydrophobic residues Phe⁶⁷ and Phe⁹³. Our approach can be adapted to other kinases and to protein enzymes in general. Once the important sites for substrate binding and dissociation are elucidated, either experimentally or computationally or both, a dissociation-resistant substrate that may act as an effective inhibitor can be designed. In summary, we present here a novel modality of GSK-3 inhibition and its potential utility for the treatment of AD and other neurological disorders.

MATERIALS AND METHODS

In vitro kinase assays

Purified GSK-3 β or GSK-3 α was incubated in a reaction mixture containing 50 mM tris-HCl (pH 7.3), 10 mM Mg(CH₃COO)₂, 100 μ M ³²P[γ -ATP] (0.5 μ Ci per assay), and 0.01% β -mercaptoethanol, together with 100 μ M indicated peptide substrate pIRS-1:RREGGMSRPAS(p)VDG, pHSF-1:RRKEEPPSPQSQ(p)P, or L807, RRKEAAPPSPQSQ(p)P for 15 min at 30°C. RR enables the binding of the peptide substrates to the p81 paper used in the next step. The reactions were spotted on p81 paper (Whatman), washed with 10 mM phosphoric acid, and counted for radioactivity. In the assays that evaluated the inhibition capability of L807 or pHSF-1, we used peptides lacking the two RR at the beginning, which prevented their binding to the p81 paper. Thus, only the RR-containing pIRS-1 bound and was detected. Selectivity of L807mts (1 μ M) was tested against 139 protein kinases (table S1). The assays were performed at the International Centre for Kinase Profiling at the Medical Research Council unit, University of Dundee, U.K.

Molecular modeling

An initial model structure of the complex GSK-3 β /ATP/2Mg²⁺/L807 was built on the basis of our previously described model of GSK-3 β /ATP/2Mg²⁺ (48), which was based on two x-ray structures: one with phosphorylated Tyr²¹⁶ (PDB ID: 11O9U) and another with a bound nonhydrolyzable analog of ATP (PDB ID: 11PYX). We extended that model by adding L807, positioned in the substrate binding cavity of GSK-3 β with Ser¹⁰(p) near the positive cavity delimited by Lys²⁰⁵, Arg⁹⁶, and Arg¹⁸⁰. The N-to-C direction of the peptide was chosen so that Ser⁶ was located roughly near the ATP groups. The complex was solvated in a box of water, neutralized, and energy-minimized. A preliminary elastic network normal modes analysis (79, 80) showed that

loops 63 to 69 and 89 to 95 of GSK-3 β are highly mobile (Fig. 2A). These loops, together with all the side chains of GSK-3 β , ATP, Mg²⁺ ions, L807, and the solvent, were free to move in the two independent 100-ns MD simulations executed for this system.

The final structures of the L807 complexes were modified by adding a phosphate group to residue Ser⁶ and omitting the terminal phosphate of ATP (replacing ATP with ADP), thus producing starting structures for the three independent 100-ns MD simulations of the DpL807 complex. Additional replacement of residue Ala³ with Glu provided starting structures for the two 100-ns simulations of the DpHSF-1 complex. The last 50 ns of each MD trajectory was considered as production trajectory and was analyzed by calculating the distributions of distances between centers of mass of groups of side chain atoms. For Lys, Arg, and Tyr(p), we separated the charged moiety from the hydrophobic part of the side chain; for Phe, Tyr, and Pro, the centers of mass of the six- or five-membered rings were used. The distances derived from the MD trajectories were compared to estimated contact distances obtained by placing residues next to each other and minimizing the energy. We used the Gromacs package for the MD simulations (81) and trajectory analyses and UCSF Chimera software for figure preparation (82).

Studies in cells

SH-SY5Y cells were grown in RPMI 1640 medium [glucose (2 mg/ml)] supplemented with 10% fetal calf serum (FCS), 5 mM L-glutamine, and 0.04% gentamicin. Cells were collected and lysed in an ice-cold buffer G (20 mM tris-HCl, 10% glycerol, 1 mM EDTA, 1 mM EGTA, 0.5% Triton X-100, 0.5 mM orthovanadate, 10 mM β -glycerophosphate, 5 mM sodium pyrophosphate, 50 mM NaF, 1 mM benzaminidine, and protease inhibitors aprotinin, leupeptin, and pepstatin A). Cell extracts were centrifuged at 14,000g for 20 min, and supernatants were collected. MEF-PS1/2^{-/-} cells were provided by B. De Strooper (KU Leuven, Belgium) (53). The cells were grown in Dulbecco's modified Eagle's medium [glucose (4.5 mg/ml)] supplemented with 10% FCS, 5 mM L-glutamine, and 1% penicillin-streptomycin. Primary cultures of CA3-CA1 hippocampal neurons were prepared from newborn mice (C57BL/6J) at postnatal day 1. In brief, brains were removed, and hippocampi were isolated and digested with buffer containing trypsin IV and deoxyribonuclease IV (Sigma). After 5 min of incubation, cells were centrifuged at 800g and plated on coverslips. After 24 hours, fresh minimum essential medium supplemented with 1% L-glutamine, 0.2% insulin, 5% fetal bovine serum, 0.1% B-27, and bovine transferrin was added. Cultures were maintained for 2 to 3 weeks.

Lysosome staining and live-cell imaging

Cells were exposed to indicated concentrations of L807mts or L803mts. Cells were then incubated with 50 nM LysoTracker Red (Molecular Probes) for 12 min at 37°C. Cells were washed twice with PBS (pH 7.4) and imaged with a laser scanning confocal microscope (Leica TCS SP5 II) with a spatial resolution of 50 to 70 nm using a 63.0 \times 1.40 oil ultraviolet objective lens.

Pharmacological studies

For stability analysis, Cy5-L807mts was incubated for varying time periods in fresh mouse serum at 37°C. The samples were separated by gel electrophoresis and imaged by an FLA-5100 analyzer (Fujifilm). Cy5-L807-mts was digested by trypsin or proteinase K at 37°C for 4 hours. For peptide delivery, Cy5-L807mts, dissolved in DDX1 solution (125 mM NaCl, 8 mM citric acid monohydrate, 15 mM Na₂HPO₄, and 0.0005% benzalkonium chloride), was administered intravenously

to five C57BL/6J mice (100 μ g per animal). After killing at the indicated times and perfusion with PBS (pH 7.4), brains were removed and immediately imaged using the CRi Maestro fluorescence imaging system. For pharmacokinetic studies, Four C57BL/6J mice were injected intravenously with Cy5-L807mts (60 μ g per animal). Blood samples were collected from the orbital vein at indicated time points. The fluorescence intensity of the serum samples were monitored by a Tecan Infinite F200 microplate fluorescence reader. In addition, serum samples were separated by gel electrophoresis and imaged by the FLA-5100 analyzer. Urine samples were collected at 10 and 12 hours after administration of Cy5-L807mts, separated by gel electrophoresis, and imaged by the FLA-5100 analyzer.

For toxicological studies, 8-week-old C57BL/6J male mice were exposed intranasally or intraperitoneally to 600 μ g of L807mts (\times 10 of optimal dose). Body weight was determined every 2 to 3 days. Animals were observed daily for clinical signs. Observations include changes in skin, fur, eyes, and mucous membranes as well as occurrence of secretions and excretions (for example, diarrhea). Changes in gait, posture, and response to handling, as well as the appearance of bizarre behavior, tremors, and seizures, over a period of 24 days were observed. The experiment included four nontreated and six L807mts-treated mice.

In vivo studies and tissue extraction

All animal experiments were performed in compliance with protocols approved by the Tel Aviv University animal care and use committee. C57BL/6J mice were treated nasally with L807mts, dissolved in DDX1 solution, at indicated concentrations for two successive days. After perfusion with saline, hippocampi were removed and immediately frozen in liquid nitrogen. A similar procedure was performed in the 5XFAD mice that were treated with L807mts. Tissues were homogenized with ice-cold buffer H [150 mM β -glycerophosphate (pH 7.3), 10% glycerol, 5 mM EGTA, 5 mM EDTA, 40 mM NaF, 25 mM sodium pyrophosphate, leupeptin, aprotinin (25 mg/ml), pepstatin A (10 mg/ml), 1 mM dithiothreitol, and 1% NP-40]. The protein extracts were centrifuged at 14,000g for 30 min, and supernatants were collected.

Western blot analyses

Equal amounts of proteins (30 to 50 μ g) were subjected to gel electrophoresis and immunoblotted with antibodies recognizing β -catenin (BD Transduction Laboratories), tau, phospho-tau (Ser³⁹⁶), β -actin, p62, LC3, and glyceraldehyde phosphate dehydrogenase (all purchased from Cell Signaling Technology) and an antibody recognizing GFAP (Sigma), followed by incubation with horseradish peroxidase-linked anti-rabbit or anti-mouse IgG (Cell Signaling Technology and Jackson ImmunoResearch, respectively).

The 5XFAD mouse model and behavior tests

5XFAD transgenic mice (60) were purchased from Jackson Laboratories. Hemizygous transgenic mice were crossed with C57BL/6J breeders as described (28, 60). Mice were housed in individual cages in a temperature-controlled facility with a 12-hour light/dark cycle. 5XFAD male mice were randomly assigned to two groups (six animals each). Mice (2 months old) were treated nasally with L807mts (60 μ g per dose), dissolved in vehicle DDX1 solution or with vehicle (referred to as "nontreated"), every other day for 120 days and as described (28). The contextual fear conditioning test was conducted as described (83). Briefly, mice were subjected to an unconditioned electric stimulus (one foot shock; 1 s/1 mA) in a training precession, and 24 hours later, a fear conditioning test was performed by scoring freezing behavior (for

example, the absence of all but respiratory movement monitored for 180 s) using a FreezeFrame automated scoring system (Coulbourn Instruments). The object recognition test was conducted as described (61, 62). In brief, 24 hours after habituation, mice were exposed to two identical objects for 5 min, and the time spent in sniffing or touching each object was measured (first session). Three hours later, the mice were exposed to one familiar and one novel object for 3 min, and the time spent near the objects was measured (second session). After 24 hours, the familiar object was replaced by a novel object, and the time spent near the objects was measured (third session). The time spent near each object was used to determine the discrimination index, calculated as the time spent near the novel object minus the time spent near the familiar object divided by the total time. Sociability was evaluated according to Crawley's sociability test using the three-chamber paradigm (68). The main principle of this test is based on the free choice of the subject mouse to spend time in any of the three boxes' compartments during two experimental sessions. Each mouse was placed in the empty three-chamber apparatus with the doors open. After habituation to the empty box, a strange mouse was placed in one of the chambers in a pencil cup. The time spent sniffing each pencil cup, the time spent in each chamber, and the number of entries into each chamber were measured.

Histology and A β staining

Saline-perfused brains were removed and fixed with 4% paraformaldehyde. Paraffin-embedded sections were cut into slices (6 μ m) and kept at 4°C. For staining, sections were deparaffinized with xylene and stained with Congo red dye (Sigma) or with an antigen-retrieval method using unmasking solution (Vector Laboratories) and antibody against A β 6E10 (Covance) or antibody GFAP antibody (Sigma). Slices were stained with secondary antibody (1:400) and visualized by fluorescence microscopy on an Olympus BX51. GFAP antibody (Sigma) was visualized by fluorescence microscopy. Quantification of A β depositions was done for the whole hippocampal area using ImageJ software (<http://imagej.nih.gov/ij/>) in an unbiased approach. Astrocytes were quantitated by measuring GFAP staining in an area measured in square pixels in the dentate gyrus and CA1 areas of the hippocampus using ImageJ software in an unbiased approach.

Statistical analyses

All experiments were repeated at least three times, and the number of animals is specified in the figure legends. Data are shown as means \pm SEM. The unpaired Student's *t* test was used for comparison of two independent groups, and one-way ANOVA followed by Dunnett's post hoc tests as outlined in each figure legend. For statistical comparisons, *P* < 0.05 was considered significant. Statistical analyses were performed with GraphPad Prism (version 7.01) software.

SUPPLEMENTARY MATERIALS

www.sciencesignaling.org/cgi/content/full/9/454/ra110/DC1

Fig. S1. RMSDs along the last 50 ns of each trajectory, calculated for the C α atoms of loop 63 to 68, loop 89 to 95, or the peptide, after superposition of the restrained C α atoms of GSK-3 β .

Fig. S2. Time dependence of the distances between selected residues in the GSK-3 β /ATP/2Mg²⁺/L807 complex.

Fig. S3. Time dependence of the distances between selected residues in the GSK-3 β /ADP/2Mg²⁺/Dpl807 complex.

Table S1. Selectivity of L807mts toward a panel of protein kinases.

Table S2. L807mts toxicology screening.

REFERENCES AND NOTES

- G. Manning, D. B. Whyte, R. Martinez, T. Hunter, S. Sudarsanam, The protein kinase complement of the human genome. *Science* **298**, 1912–1934 (2002).
- J. Bain, H. McLauchlan, M. Elliott, P. Cohen, The specificities of protein kinase inhibitors: An update. *Biochem. J.* **371**, 199–204 (2003).
- J. Bain, L. Plater, M. Elliott, N. Shpuro, C. J. Hastie, H. McLauchlan, I. Klevernic, J. S. Arthur, D. R. Alessi, P. Cohen, The selectivity of protein kinase inhibitors: A further update. *Biochem. J.* **408**, 297–315 (2007).
- S. K. Hanks, A. M. Quinn, T. Hunter, The protein kinase family: Conserved features and deduced phylogeny of the catalytic domains. *Science* **241**, 42–52 (1988).
- S. S. Taylor, E. Radzio-Andzelm, T. Hunter, How do protein kinases discriminate between serine/threonine and tyrosine? Structural insights from the insulin receptor protein-tyrosine kinase. *FASEB J.* **9**, 1255–1266 (1995).
- B. E. Kemp, R. B. Pearson, C. M. House, Pseudosubstrate-based peptide inhibitors. *Methods Enzymol.* **201**, 287–304 (1991).
- T. R. Soderling, Protein kinases. Regulation by autoinhibitory domains. *J. Biol. Chem.* **265**, 1823–1826 (1990).
- T. Eichholtz, D. B. A. de Bont, J. de Widt, R. M. J. Liskamp, H. L. Ploegh, A myristoylated pseudosubstrate peptide, a novel protein kinase C inhibitor. *J. Biol. Chem.* **268**, 1982–1986 (1993).
- D. A. Brickey, J. G. Bann, Y.-L. Fong, L. Perrino, R. G. Brennan, T. R. Soderling, Mutational analysis of the autoinhibitory domain of calmodulin kinase II. *J. Biol. Chem.* **269**, 29047–29054 (1994).
- C. T. Wlash, Suicide substrates, mechanism-based inactivators: Recent developments. *Annu. Rev. Biochem.* **53**, 493–535 (1984).
- H. Eldar-Finkelman, A. Martinez, GSK-3 inhibitors: Preclinical and clinical focus on CNS. *Front. Mol. Neurosci.* **4**, 32 (2011).
- M. K. King, M. Pardo, Y. Cheng, K. Downey, R. S. Jope, E. Beurel, Glycogen synthase kinase-3 inhibitors: Rescuers of cognitive impairments. *Pharmacol. Ther.* **141**, 1–12 (2014).
- M. Llorens-Martin, J. Jurado, F. Hernández, J. Ávila, GSK-3 β , a pivotal kinase in Alzheimer disease. *Front. Mol. Neurosci.* **7**, 46 (2014).
- S. H. Liang, J. M. Chen, M. D. Normandin, J. S. Chang, G. C. Chang, C. K. Taylor, P. Trapa, M. S. Plummer, K. S. Para, E. L. Conn, L. Lopresti-Morrow, L. F. Lanyon, J. M. Cook, K. E. G. Richter, C. E. Nolan, J. B. Schachter, F. Janat, Y. Che, V. Shanmugasundaram, B. A. Lefker, B. E. Enerson, E. Livni, L. Wang, N. J. Guehl, D. Patnaik, F. F. Wagner, R. Perlis, E. B. Holson, S. J. Haggarty, G. El Fakhri, R. G. Kurumbail, N. Vasdev, Discovery of a highly selective glycogen synthase kinase-3 inhibitor (PF-04802367) that modulates tau phosphorylation in the brain: Translation for PET neuroimaging. *Angew. Chem. Int. Ed. Engl.* **55**, 9601–9605 (2016).
- F. F. Wagner, J. A. Bishop, J. P. Gale, X. Shi, M. Walk, J. Ketterman, D. Patnaik, D. Barker, D. Walpita, A. J. Campbell, S. Nguyen, M. Lewis, L. Ross, M. Weiwier, W. F. An, A. R. Germain, P. P. Nag, S. Metkar, T. Kaya, S. Dandapani, D. E. Olson, A.-L. Barbe, F. Lazzaro, J. R. Sacher, J. H. Cheah, D. Fei, J. Perez, B. Munoz, M. Palmer, K. Stegmaier, S. L. Schreiber, E. Scolnick, Y.-L. Zhang, S. J. Haggarty, E. B. Holson, J. Q. Pan, Inhibitors of glycogen synthase kinase 3 with exquisite kinase-wide selectivity and their functional effects. *ACS Chem. Biol.* **11**, 1952–1963 (2016).
- J. R. Woodgett, Molecular cloning and expression of glycogen synthase kinase-3/factor A. *EMBO J.* **9**, 2431–2438 (1990).
- D. P. Hanger, K. Hughes, J. R. Woodgett, J.-P. Brion, B. H. Anderton, Glycogen synthase kinase-3 induces Alzheimer's disease-like phosphorylation of tau: Generation of paired helical filament epitopes and neuronal localisation of the kinase. *Neurosci. Lett.* **147**, 58–62 (1992).
- T. Li, C. Hawkes, H. Y. Qureshi, S. Kar, H. K. Paudel, Cyclin-dependent protein kinase 5 primes microtubule-associated protein tau site-specifically for glycogen synthase kinase 3 β . *Biochemistry* **45**, 3134–3145 (2006).
- M. G. Spillantini, M. Goedert, Tau pathology and neurodegeneration. *Lancet Neurol.* **12**, 609–622 (2013).
- M. R. Khanna, J. Kovalevich, V. M.-Y. Lee, J. Q. Trojanowski, K. R. Brunden, Therapeutic strategies for the treatment of tauopathies: Hopes and challenges. *Alzheimers Dement.* **12**, 1051–1065 (2016).
- S. Ikeda, S. Kishida, H. Yamamoto, H. Murai, S. Koyama, A. Kikuchi, Axin, a negative regulator of the Wnt signaling pathway, forms a complex with GSK-3 β and β -catenin and promotes GSK-3 β -dependent phosphorylation of β -catenin. *EMBO J.* **17**, 1371–1384 (1998).
- C. Yost, M. Torres, J. R. Miller, E. Huang, D. Kimelman, R. T. Moon, The axis-inducing activity, stability, and subcellular distribution of β -catenin is regulated in *Xenopus* embryos by glycogen synthase kinase 3. *Genes Dev.* **10**, 1443–1454 (1996).
- K. P. Hoefflich, J. Luo, E. A. Rubie, M.-S. Tsao, O. Jin, J. R. Woodgett, Requirement for glycogen synthase kinase-3 β in cell survival and NF- κ B activation. *Nature* **406**, 86–90 (2000).
- K. A. Steinbrecher, W. Wilson III, P. C. Cogswell, A. S. Baldwin, Glycogen synthase kinase 3 β functions to specify gene-specific, NF- κ B-dependent transcription. *Mol. Cell. Biol.* **25**, 8444–8455 (2005).

25. M. Martin, K. Rehani, R. S. Jope, S. M. Michalek, Toll-like receptor-mediated cytokine production is differentially regulated by glycogen synthase kinase 3. *Nat. Immunol.* **6**, 777–784 (2005).
26. A. V. Ougolkov, M. E. Fernandez-Zapico, D. N. Savoy, R. A. Urrutia, D. D. Billadeau, Glycogen synthase kinase-3 β participates in nuclear factor κ B-mediated gene transcription and cell survival in pancreatic cancer cells. *Cancer Res.* **65**, 2076–2081 (2005).
27. I. Azoulay-Alfaguter, R. Elya, L. Avrahami, A. Katz, H. Eldar-Finkelman, Combined regulation of mTORC1 and lysosomal acidification by GSK-3 suppresses autophagy and contributes to cancer cells growth. *Oncogene* **34**, 4613–4623 (2015).
28. L. Avrahami, D. Farfara, M. Shaham-Kol, R. Vassar, D. Frenkel, H. Eldar-Finkelman, Inhibition of glycogen synthase kinase-3 ameliorates β -amyloid pathology and restores lysosomal acidification and mTOR activity in the Alzheimer's disease mouse model: In vivo and in vitro studies. *J. Biol. Chem.* **288**, 1295–1306 (2013).
29. A. V. Franklin, M. K. King, V. Palomo, A. Martinez, L. L. McMahon, R. S. Jope, Glycogen synthase kinase-3 inhibitors reverse deficits in long-term potentiation and cognition in fragile X mice. *Biol. Psychiatry* **75**, 198–206 (2014).
30. E. Beurel, O. Kaidanovich-Beilin, W.-I. Yeh, L. Song, V. Palomo, S. M. Michalek, J. R. Woodgett, L. E. Harrington, H. Eldar-Finkelman, A. Martinez, R. S. Jope, Regulation of Th1 cells and experimental autoimmune encephalomyelitis by glycogen synthase kinase-3. *J. Immunol.* **190**, 5000–5011 (2013).
31. P. T. T. Ly, Y. Wu, H. Zou, R. Wang, W. Zhou, A. Kinoshita, M. Zhang, Y. Yang, F. Cai, J. Woodgett, W. Song, Inhibition of GSK3 β -mediated BACE1 expression reduces Alzheimer-associated phenotypes. *J. Clin. Invest.* **123**, 224–235 (2013).
32. L. Serenó, M. Coma, M. Rodríguez, P. Sánchez-Ferrer, M. B. Sánchez, I. Gich, J. M. Agulló, M. Pérez, J. Avila, C. Guardia-Laguarta, J. Clarimón, A. Lleó, T. Gómez-Isla, A novel GSK-3 β inhibitor reduces Alzheimer's pathology and rescues neuronal loss in vivo. *Neurobiol. Dis.* **35**, 359–367 (2009).
33. T. Engel, F. Hernández, J. Avila, J. J. Lucas, Full reversal of Alzheimer's disease-like phenotype in a mouse model with conditional overexpression of glycogen synthase kinase-3. *J. Neurosci.* **26**, 5083–5090 (2006).
34. J. Carmichael, K. L. Sugars, Y. P. Bao, D. C. Rubinsztein, Glycogen synthase kinase-3 β inhibitors prevent cellular polyglutamine toxicity caused by the Huntington's disease mutation. *J. Biol. Chem.* **277**, 33791–33798 (2002).
35. J. Avila, F. Wandosell, F. Hernández, Role of glycogen synthase kinase-3 in Alzheimer's disease pathogenesis and glycogen synthase kinase-3 inhibitors. *Expert Rev. Neurother.* **10**, 703–710 (2010).
36. C. Hooper, R. Killick, S. Lovestone, The GSK3 hypothesis of Alzheimer's disease. *J. Neurochem.* **104**, 1433–1439 (2008).
37. D. E. Hurtado, L. Molina-Porcel, J. C. Carroll, C. MacDonald, A. K. Aboagye, J. Q. Trojanowski, V. M.-Y. Lee, Selectively silencing GSK-3 isoforms reduces plaques and tangles in mouse models of Alzheimer's disease. *J. Neurosci.* **32**, 7392–7402 (2012).
38. B. Plotkin, O. Kaidanovich, I. Talior, H. Eldar-Finkelman, Insulin mimetic action of synthetic phosphorylated peptide inhibitors of glycogen synthase kinase-3. *J. Pharmacol. Exp. Ther.* **305**, 974–980 (2003).
39. C. J. Fiol, A. M. Mahrenholz, Y. Wang, R. W. Roeske, P. J. Roach, Formation of protein kinase recognition sites by covalent modification of the substrate. Molecular mechanism for the synergistic action of casein kinase II and glycogen synthase kinase 3. *J. Biol. Chem.* **262**, 14042–14048 (1987).
40. J. R. Woodgett, P. Cohen, Multisite phosphorylation of glycogen synthase. Molecular basis for the substrate specificity of glycogen synthase kinase-3 and casein kinase-II (glycogen synthase kinase-5). *Biochim. Biophys. Acta* **788**, 339–347 (1984).
41. B. Chu, F. Soncin, B. D. Price, M. A. Stevenson, S. K. Calderwood, Sequential phosphorylation by mitogen-activated protein kinase and glycogen synthase kinase 3 represses transcriptional activation by heat shock factor-1. *J. Biol. Chem.* **271**, 30847–30857 (1996).
42. O. Kaidanovich-Beilin, H. Eldar-Finkelman, Long-term treatment with novel glycogen synthase kinase-3 inhibitor improves glucose homeostasis in ob/ob mice: Molecular characterization in liver and muscle. *J. Pharmacol. Exp. Ther.* **316**, 17–24 (2006).
43. R. Rao, C.-M. Hao, R. Redha, D. H. Wasserman, O. P. McGuinness, M. D. Breyer, Glycogen synthase kinase 3 inhibition improves insulin-stimulated glucose metabolism but not hypertension in high-fat-fed C57BL/6J mice. *Diabetologia* **50**, 452–460 (2007).
44. O. Kaidanovich-Beilin, A. Milman, A. Weizman, C. G. Pick, H. Eldar-Finkelman, Rapid anti-depressive like activity of specific glycogen synthase kinase-3 inhibitor, and its effect on β -catenin in the mouse hippocampus. *Biol. Psychiatry* **55**, 781–784 (2004).
45. Q. Zhu, J. Yang, S. Han, J. Liu, J. Holzbeierlein, J. B. Thrasher, B. Li, Suppression of glycogen synthase kinase 3 activity reduces tumor growth of prostate cancer in vivo. *Prostate* **71**, 835–845 (2011).
46. G. Chen, K. A. Bower, C. Ma, S. Fang, C. J. Thiele, J. Luo, Glycogen synthase kinase 3 β (GSK3 β) mediates 6-hydroxydopamine-induced neuronal death. *FASEB J.* **18**, 1162–1164 (2004).
47. A. Licht-Murava, B. Plotkin, M. Eisenstein, H. Eldar-Finkelman, Elucidating substrate and inhibitor binding sites on the surface of GSK-3 β and the refinement of a competitive inhibitor. *J. Mol. Biol.* **408**, 366–378 (2011).
48. R. Ilouz, N. Kowelsman, M. Eisenstein, H. Eldar-Finkelman, Identification of novel glycogen synthase kinase-3 β substrate-interacting residues suggests a common mechanism for substrate recognition. *J. Biol. Chem.* **281**, 30621–30630 (2006).
49. Z. Liberman, H. Eldar-Finkelman, Serine 332 phosphorylation of insulin receptor substrate-1 by glycogen synthase kinase-3 attenuates insulin signaling. *J. Biol. Chem.* **280**, 4422–4428 (2005).
50. R. Dajani, E. Fraser, S. M. Roe, N. Young, V. Good, T. C. Dale, L. H. Pearl, Crystal structure of glycogen synthase kinase 3 β : Structural basis for phosphate-primed substrate specificity and autoinhibition. *Cell* **105**, 721–732 (2001).
51. E. ter Haar, J. T. Coll, D. A. Austen, H.-M. Hsiao, L. Swenson, J. Jain, Structure of GSK3 β reveals a primed phosphorylation mechanism. *Nat. Struct. Biol.* **8**, 593–596 (2001).
52. B. Rubinfeld, I. Albert, E. Porfiri, C. Fiol, S. Munemitsu, P. Polakis, Binding of GSK3 β to the APC- β -catenin complex and regulation of complex assembly. *Science* **272**, 1023–1026 (1996).
53. A. Herreman, G. Van Gassen, M. Bentahir, O. Nyabi, K. Craessaerts, U. Mueller, W. Annaert, B. De Strooper, γ -Secretase activity requires the presenilin-dependent trafficking of nicastrin through the Golgi apparatus but not its complex glycosylation. *J. Cell Sci.* **116**, 1127–1136 (2003).
54. J.-H. Lee, W. H. Yu, A. Kumar, S. Lee, P. S. Mohan, C. M. Peterhoff, D. M. Wolfe, M. Martinez-Vicente, A. C. Massey, G. Sovak, Y. Uchiyama, D. Westaway, A. M. Cuervo, R. A. Nixon, Lysosomal proteolysis and autophagy require presenilin 1 and are disrupted by Alzheimer-related PS1 mutations. *Cell* **141**, 1146–1158 (2010).
55. J. Born, T. Lange, W. Kern, G. P. McGregor, U. Bickel, H. L. Fehm, Sniffing neuropeptides: A transnasal approach to the human brain. *Nat. Neurosci.* **5**, 514–516 (2002).
56. L. Illum, Transport of drugs from the nasal cavity to the central nervous system. *Eur. J. Pharm. Sci.* **11**, 1–18 (2000).
57. T. Li, H. K. Paudel, Glycogen synthase kinase 3 β phosphorylates Alzheimer's disease-specific Ser³⁹⁶ of microtubule-associated protein tau by a sequential mechanism. *Biochemistry* **45**, 3125–3133 (2006).
58. D. P. Hanger, B. H. Anderton, W. Noble, Tau phosphorylation: The therapeutic challenge for neurodegenerative disease. *Trends Mol. Med.* **15**, 112–119 (2009).
59. H. Rosenmann, N. Grigoriadis, H. Eldar-Levy, A. Avital, L. Rozenstein, O. Touloumi, L. Behar, T. Ben-Hur, Y. Avraham, E. Berry, M. Segal, I. Ginzburg, O. Abramsky, A novel transgenic mouse expressing double mutant tau driven by its natural promoter exhibits tauopathy characteristics. *Exp. Neurol.* **212**, 71–84 (2008).
60. H. Oakley, S. L. Cole, S. Logan, E. Maus, P. Shao, J. Craft, A. Guillozet-Bongaarts, M. Ohno, J. Disterhoft, L. Van Eldik, R. Berry, R. Vassar, Intraneuronal β -amyloid aggregates, neurodegeneration, and neuron loss in transgenic mice with five familial Alzheimer's disease mutations: Potential factors in amyloid plaque formation. *J. Neurosci.* **26**, 10129–10140 (2006).
61. M. Leger, A. Quideville, V. Bouet, B. Haelewyn, M. Boulouard, P. Schumann-Bard, T. Freret, Object recognition test in mice. *Nat. Protoc.* **8**, 2531–2537 (2013).
62. R. A. Bevins, J. Besheer, Object recognition in rats and mice: A one-trial non-matching-to-sample learning task to study 'recognition memory'. *Nat. Protoc.* **1**, 1306–1311 (2006).
63. G. Cipriani, M. Vedovello, M. Ulivi, A. Nuti, C. Lucetti, Repetitive and stereotypic phenomena and dementia. *Am. J. Alzheimers Dis. Other Demen.* **28**, 223–227 (2013).
64. M. Langen, M. J. H. Kas, W. G. Staal, H. van Engeland, S. Durston, The neurobiology of repetitive behavior: Of mice.... *Neurosci. Biobehav. Rev.* **35**, 345–355 (2011).
65. M. A. Mines, C. J. Yuskaitis, M. K. King, E. Beurel, R. S. Jope, GSK3 influences social preference and anxiety-related behaviors during social interaction in a mouse model of fragile X syndrome and autism. *PLOS ONE* **5**, e9706 (2010).
66. C. J. Yuskaitis, M. A. Mines, M. K. King, J. D. Sweatt, C. A. Miller, R. S. Jope, Lithium ameliorates altered glycogen synthase kinase-3 and behavior in a mouse model of fragile X syndrome. *Biochem. Pharmacol.* **79**, 632–646 (2010).
67. O. Kaidanovich-Beilin, T. V. Lipina, K. Takao, M. van Eede, S. Hattori, C. Laliberté, M. Khan, K. Okamoto, J. W. Chambers, P. J. Fletcher, K. MacAulay, B. W. Doble, M. Henkelman, T. Miyakawa, J. Roder, J. R. Woodgett, Abnormalities in brain structure and behavior in GSK-3 α mutant mice. *Mol. Brain* **2**, 35 (2009).
68. J. J. Nadler, S. S. Moy, G. Dold, D. Trang, N. Simmons, A. Perez, N. B. Young, R. P. Barbaro, J. Piven, T. R. Magnuson, J. N. Crawley, Automated apparatus for quantitation of social approach behaviors in mice. *Genes Brain Behav.* **3**, 303–314 (2004).
69. J. N. Crawley, T. Chen, A. Puri, R. Washburn, T. L. Sullivan, J. H. Mill, N. B. Young, J. J. Nadler, S. S. Moy, L. J. Young, H. K. Caldwell, W. S. Young, Social approach behaviors in oxytocin knockout mice: Comparison of two independent lines tested in different laboratory environments. *Neuropeptides* **41**, 145–163 (2007).
70. D. J. Selkoe, Alzheimer's disease: Genes, proteins, and therapy. *Physiol. Rev.* **81**, 741–766 (2001).
71. B. De Strooper, Proteases and proteolysis in Alzheimer disease: A multifactorial view on the disease process. *Physiol. Rev.* **90**, 465–494 (2010).
72. J. Hardy, The amyloid hypothesis for Alzheimer's disease: A critical reappraisal. *J. Neurochem.* **110**, 1129–1134 (2009).
73. R. A. Nixon, The role of autophagy in neurodegenerative disease. *Nat. Med.* **19**, 983–997 (2013).
74. D. C. Rubinsztein, P. Codogno, B. Levine, Autophagy modulation as a potential therapeutic target for diverse diseases. *Nat. Rev. Drug Discov.* **11**, 709–730 (2012).

75. D. Klionsky, An overview of autophagy: Morphology, mechanism and regulation. *Antioxid. Redox Signal.* (2013).
76. D. A. DeWitt, G. Perry, M. Cohen, C. Doller, J. Silver, Astrocytes regulate microglial phagocytosis of senile plaque cores of Alzheimer's disease. *Exp. Neurol.* **149**, 329–340 (1998).
77. B. Webster, L. Hansen, A. Adame, L. Crews, M. Torrance, L. Thal, E. Masliah, Astroglial activation of extracellular-regulated kinase in early stages of Alzheimer disease. *J. Neuropathol. Exp. Neurol.* **65**, 142–151 (2006).
78. A. M. Birch, The contribution of astrocytes to Alzheimer's disease. *Biochem. Soc. Trans.* **42**, 1316–1320 (2014).
79. M. M. Tirion, Large amplitude elastic Motions in proteins from a single-parameter, atomic analysis. *Phys. Rev. Lett.* **77**, 1905–1908 (1996).
80. K. Suhre, Y.-H. Sanejouand, *ElNémo*: A normal mode web server for protein movement analysis and the generation of templates for molecular replacement. *Nucleic Acids Res.* **32**, W610–W614 (2004).
81. D. Van Der Spoel, E. Lindahl, B. Hess, G. Groenhof, A. E. Mark, H. J. C. Berendsen, GROMACS: Fast, flexible, and free. *J. Comput. Chem.* **26**, 1701–1718 (2005).
82. E. F. Pettersen, T. D. Goddard, C. C. Huang, G. S. Couch, D. M. Greenblatt, E. C. Meng, T. E. Ferrin, UCSF Chimera—A visualization system for exploratory research and analysis. *J. Comput. Chem.* **25**, 1605–1612 (2004).
83. M. Ohno, L. Chang, W. Tseng, H. Oakley, M. Citron, W. L. Klein, R. Vassar, J. F. Disterhoft, Temporal memory deficits in Alzheimer's mouse models: Rescue by genetic deletion of BACE1. *Eur. J. Neurosci.* **23**, 251–260 (2006).

Acknowledgments: We thank I. Slutski for the assistance in the primary neurons studies, I. Gozes for the assistance in the animal behavior studies, H. Rosenman for providing the transgenic tau mice, B. De Strooper for providing MEF-PS1/2^{-/-} cells, and D. Shabat for providing Cy5-L807mts. **Funding:** This work was supported by the Colton-Nadal Fund at Tel Aviv University and the Israeli Chief Scientist Office Project #51381. **Author contributions:** A.L.-M. and R.P. designed and performed the in vitro and in vivo experiments. L.V. designed, performed, and analyzed the pharmacological experiments. L.A. and B.P. conducted experiments in cells. M.E. designed and conducted the computational studies, analyzed the results, and wrote the computational part in the manuscript. H.E.-F. supervised the project, designed experiments, analyzed the data, and wrote the manuscript. **Competing interests:** The authors declare that they have no competing interests. **Data and materials availability:** All data and reagents are available upon request from our laboratory. L807mts is patented (PCT/IL2014/050567).

Submitted 3 August 2016

Accepted 27 October 2016

Published 15 November 2016

10.1126/scisignal.aah71102

Citation: A. Licht-Murava, R. Paz, L. Vaks, L. Avrahami, B. Plotkin, M. Eisenstein, H. Eldar-Finkelman, A unique type of GSK-3 inhibitor brings new opportunities to the clinic. *Sci. Signal.* **9**, ra110 (2016).

A unique type of GSK-3 inhibitor brings new opportunities to the clinic

Avital Licht-Murava, Rom Paz, Lilach Vaks, Limor Avrahami, Batya Plotkin, Miriam Eisenstein and Hagit Eldar-Finkelman (November 15, 2016)

Science Signaling **9** (454), ra110. [doi: 10.1126/scisignal.aah7102]

The following resources related to this article are available online at <http://stke.sciencemag.org>. This information is current as of November 19, 2016.

- Article Tools** Visit the online version of this article to access the personalization and article tools:
<http://stke.sciencemag.org/content/9/454/ra110>
- Supplemental Materials** "*Supplementary Materials*"
<http://stke.sciencemag.org/content/suppl/2016/11/11/9.454.ra110.DC1>
- Related Content** The editors suggest related resources on *Science's* sites:
<http://stke.sciencemag.org/content/sigtrans/9/454/eg10.full>
<http://stke.sciencemag.org/content/sigtrans/9/427/ra47.full>
<http://stke.sciencemag.org/content/sigtrans/8/389/ec223.abstract>
<http://stke.sciencemag.org/content/sigtrans/9/419/ec58.abstract>
<http://stke.sciencemag.org/content/sigtrans/9/450/pe3.full>
<http://stm.sciencemag.org/content/scitransmed/7/278/278ra33.full>
<http://stke.sciencemag.org/content/sigtrans/9/454/pc22.full>
<http://advances.sciencemag.org/content/advances/2/8/e1600947.full>
- References** This article cites 83 articles, 32 of which you can access for free at:
<http://stke.sciencemag.org/content/9/454/ra110#BIBL>
- Permissions** Obtain information about reproducing this article:
<http://www.sciencemag.org/about/permissions.dtl>